

Pressure-induced crystallization of an amorphous martensite alloy

HPSTAR
1044-2020

Cite as: J. Appl. Phys. 128, 085901 (2020); doi: 10.1063/5.0015076

Submitted: 24 May 2020 · Accepted: 7 August 2020 ·

Published Online: 24 August 2020



View Online



Export Citation



CrossMark

Ye Liu,¹ Hongbo Lou,¹ Fei Zhang,^{1,2} Tao Liang,^{1,3} Songyi Chen,¹ Shubin Li,^{1,4} Xin Zhang,¹ Lijie Tan,^{1,5} Vitali B. Prakapenka,⁶ Eran Greenberg,⁶ Yanping Yang,¹ Zhidan Zeng,¹ and Qiaoshi Zeng^{1,3,a)}

AFFILIATIONS

¹Center for High Pressure Science and Technology Advanced Research (HPSTAR), Pudong, Shanghai 201203, People's Republic of China²State Key Laboratory for Advanced Metals and Materials, University of Science and Technology Beijing, Beijing 100083, People's Republic of China³Jiangsu Key Laboratory of Advanced Metallic Materials, School of Materials Science and Engineering, Southeast University, Nanjing 211189, People's Republic of China⁴School of Physics and Astronomy, Shanghai Jiao Tong University, Shanghai 200240, People's Republic of China⁵Institute of Atomic and Molecular Physics, Sichuan University, Chengdu 610065, China⁶Center for Advanced Radiation Sources, University of Chicago, Chicago, Illinois 60637, USA^{a)}Author to whom correspondence should be addressed: zengqs@hpstar.ac.cn

ABSTRACT

Recently, solid-state amorphization through temperature-induced martensitic transition has been reported. The stability of the amorphous martensite phase, which co-exists with a crystalline counterpart, is intriguing but remains unclear. In this work, we studied the structural stability of a $\text{Ti}_{59.1}\text{Zr}_{37}\text{Cu}_{2.3}\text{Fe}_{1.6}$ amorphous martensite alloy by combining *in situ* high-pressure synchrotron x-ray diffraction with *ex situ* transmission electron microscopy. During compression at room temperature, an irreversible pressure-induced crystallization of the amorphous martensite phase into a β -Ti phase is revealed. Qualitative analysis reveals the important role of the local atomic strain in stabilizing/destabilizing amorphous martensite alloys and its high tunability of the local atomic strain under high pressure.

Published under license by AIP Publishing. <https://doi.org/10.1063/5.0015076>

I. INTRODUCTION

By cooling an alloy melt fast enough, crystallization could be bypassed by forming an amorphous alloy (also often referred to as metallic glass). With a combination of non-directional metallic bonding and densely packed disordered structure, amorphous alloys obviously set themselves apart from both conventional crystalline metals and oxide glasses, owing to their extraordinary unique mechanical and chemical properties and potential in widespread applications.^{1–6} However, the forming of amorphous alloys prepared by melt-quenching usually requires a high cooling rate, which limits the maximum sample size (thickness).⁷ Therefore, intense efforts have been devoted to overcome the size limitation of amorphous alloys in casting by searching for new compositions with lower critical cooling rates.^{8,9} Meanwhile, other synthesis means such as solid-state amorphization (SSA) including pressure-induced

amorphization, mechanical alloying, and hydrogen absorption also attracted considerable attention.^{10–18}

Recently, Zhang *et al.*¹⁹ reported a new way of forming amorphous alloys via a so-called martensite amorphization mechanism. During cooling $\text{Ti}_{59.1}\text{Zr}_{37}\text{Cu}_{2.3}\text{X}_{1.6}$ ($\text{X} = \text{Fe}, \text{Co},$ and Ni) alloys, the high temperature metastable β -Ti phases ($\text{Im}\bar{3}\text{m}$) could not transform into their typical α' ($\text{P}6_3/\text{mmc}$), α'' (Cmcm), or ω ($\text{P}6/\text{mmm}$) martensites due to high local elastic strain energy that impedes the ideal cooperative movement of atoms; instead, a thermodynamically more favorable amorphous phase forms via local lattice shear and distortion accompanied by heat release. Moreover, the amorphous phase has a regular morphology of an intragranular lenticular and co-exists with the metastable β -Ti phase. When heated high enough, the amorphous phase will transform back into a pure β -Ti phase again (amorphous $\rightarrow \alpha \rightarrow \beta$). Conventional amorphous alloys

usually require a fast enough cooling rate to kinetically trap their melts into non-equilibrium amorphous states. In contrast, the martensite amorphization is surprisingly insensitive to cooling rates. Moreover, it only exists in a very narrow composition range with an appropriate content of β phase stabilizers.¹⁹ These facts indicate that the amorphous martensite alloy is quite unique compared to other conventional amorphous materials and worth more investigation.

Through a systematical study in a relatively wide composition and temperature space, Zhang *et al.*¹⁹ explicitly reveal an alternative SSA mechanism via martensitic transformations. However, the co-existence of the “stable” amorphous phase and the metastable β -Ti phase in those alloys over a large temperature range raises an intriguing question regarding the relative stabilities of those phases of the Ti alloys. The phase transitions of pure Ti have been extensively studied, and the stabilities of its various phases have been addressed in a pressure–temperature phase diagram of up to 200 GPa and ~ 3500 K.²⁰ In contrast, phase transitions in Ti alloys²¹ are much more complex and richer because samples with modified compositions or prepared by diverse methods usually have different initial phases.^{22–24} Zeng *et al.*^{25,26} found that a $\text{Ce}_{75}\text{Al}_{25}$ amorphous alloy can devitrify into a face-centered cubic (fcc) single crystal at ~ 25 GPa and room temperature, linking an amorphous structure and a crystal structure through polymorphic transition. The pressure-induced change of local atomic strain and stress is believed to play a vital role in the devitrification of the $\text{Ce}_{75}\text{Al}_{25}$ alloy.^{25,26} Therefore, pressure could be an interesting parameter as well to study the $\text{Ti}_{59.1}\text{Zr}_{37}\text{Cu}_{2.3}\text{X}_{1.6}$ (X = Fe, Co, and Ni) alloys in order to clarify the effect of local elastic strain, deepen our understanding of the formation of the martensite amorphous phase, and address its stability with respect to other competing crystalline counterparts.

In this work, we choose a $\text{Ti}_{59.1}\text{Zr}_{37}\text{Cu}_{2.3}\text{Fe}_{1.6}$ alloy as a model system and employ *in situ* high-pressure synchrotron x-ray diffraction (XRD) to characterize the structural stability and evolution of the martensite amorphous $\text{Ti}_{59.1}\text{Zr}_{37}\text{Cu}_{2.3}\text{Fe}_{1.6}$ alloy up to ~ 40 GPa in a diamond anvil cell (DAC) during compression and following decompression.²⁷ The initial sample and samples after high-pressure experiments are also characterized by *ex situ* transmission electron microscopy (TEM). The instability under high pressure and an irreversible pressure-induced crystallization of the amorphous martensite phase are revealed and discussed.

II. EXPERIMENTS

A. Materials and methods

A master ingot of the $\text{Ti}_{59.1}\text{Zr}_{37}\text{Cu}_{2.3}\text{Fe}_{1.6}$ alloy was prepared by arc-melting a mixture of high-purity Ti (99.995 at. %), Zr (99.9 at. %), Cu (99.999 at. %), and Fe (99.99 at. %) metals in a Ti-gettered high-purity argon atmosphere. The ingot was remelted four times to reach chemical homogeneity. Ribbons with a thickness of ~ 0.2 mm were further prepared from the master ingot by a melt-spinning technique. The results of XRD and differential scanning calorimeter (DSC) measurements of the ribbon sample coincide with the previous report in the literature.¹⁹

B. Sample loading for high-pressure experiments

A symmetric DAC with a culet size of ~ 400 μm was used to generate high pressure for *in situ* XRD experiments.²⁸ The sample chamber was a hole (~ 150 μm in diameter and ~ 47 μm in thickness) drilled by a laser in the center of an indent (pre-indented to ~ 20 GPa) of a T301 stainless steel gasket. The ribbon sample was cut into small flakes with an area of $\sim 50 \times 50$ μm^2 and a thickness of ~ 30 μm and then loaded into a DAC. A tiny piece of gold foil (~ 4 μm in thickness) with an area of $\sim 10 \times 10$ μm^2 was loaded along with the sample as a pressure standard.²⁹ Silicone oil and 4:1 methanol-ethanol mixture were used as the pressure medium to provide a quasi-hydrostatic pressure environment for *in situ* high-pressure XRD and *ex situ* high-pressure TEM characterizations, respectively.³⁰

C. Synchrotron radiation XRD experiments

Synchrotron radiation XRD experiments at ambient conditions on the $\text{Ti}_{59.1}\text{Zr}_{37}\text{Cu}_{2.3}\text{Fe}_{1.6}$ alloy sample were performed at the beamline 12.2.2 at the Advanced Light Source (ALS), Lawrence Berkeley National Laboratory (LBNL), USA. The x-ray wavelength was 0.5391 Å, and the beam size was $\sim 10 \times 10$ μm^2 . *In situ* high-pressure XRD experiments were performed at the beamline 13-ID-D at Advanced Photon Source (APS), Argonne National Laboratory (ANL), USA. The x-ray wavelength was 0.3220 Å, and the beam size was $\sim 3 \times 4$ μm^2 . With the small x-ray beam size, XRD could be taken separately on the sample, gold, and background without interference from each other. A MAR345 image plate and a MAR165 charge-coupled device (CCD) detectors were used for data collection at ALS and APS, respectively.

D. TEM experiments

As-prepared ribbon samples and samples recovered from high-pressure experiments were all cut using a focused ion beam (FEI Versa 3D) for TEM measurements with a sample size of $\sim 2 \times 10$ μm^2 and a thickness of ~ 200 nm. The high-resolution transmission electron microscopy (HRTEM) images and selected area electron diffraction (SAED) images were collected using a Tecnai F20 (FEI) TEM operated at 200 keV.

III. RESULTS AND DISCUSSION

The structure of the as-prepared sample was carefully characterized to make sure it reproduces the results reported in Ref. 19, showing a co-existence of an amorphous phase and a crystalline β -Ti phase. Figure 1(a) presents the synchrotron XRD result of the as-prepared $\text{Ti}_{59.1}\text{Zr}_{37}\text{Cu}_{2.3}\text{Fe}_{1.6}$ alloy sample at ambient conditions. The integrated XRD pattern of the alloy contains sharp Bragg peaks and a relatively weak and broad amorphous-like diffuse peak, where the latter is fitted using the Voigt function profile, as shown in orange. All the sharp Bragg peaks can be well indexed into a β -Ti phase, which has a body-centered cubic (bcc) structure with the space group of (Im $\bar{3}$ m) and the unit cell parameter $a = 3.393(2)$ Å.

Synchrotron XRD provides the overall structural information of the bulk sample. The x-ray beam sizes and the sample thickness on the x-ray beam path we used are much larger than the

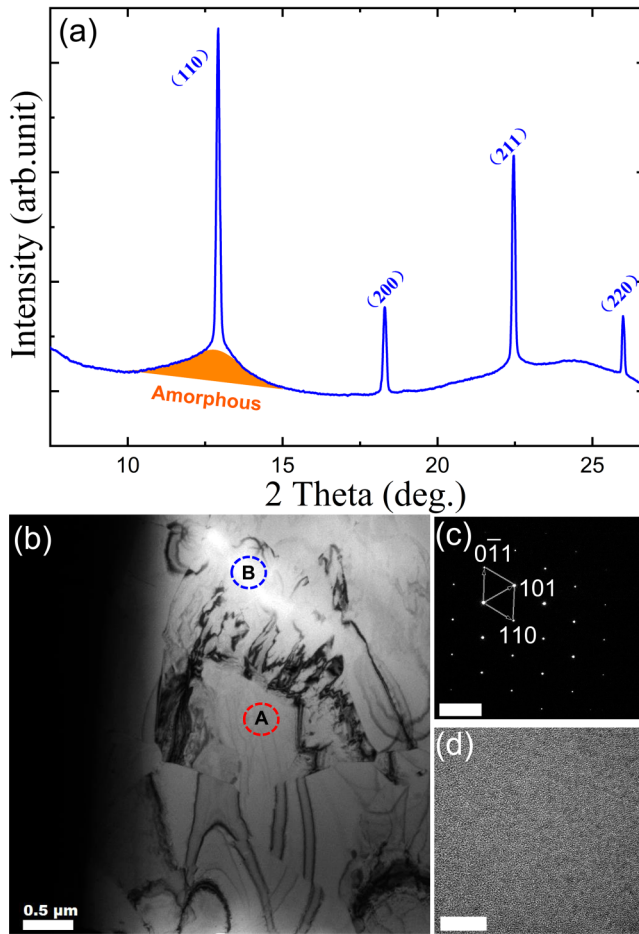


FIG. 1. Characterization of the microscopic structure of the as-prepared $\text{Ti}_{59.1}\text{Zr}_{37}\text{Cu}_{2.3}\text{Fe}_{1.6}$ alloy sample. (a) Synchrotron XRD pattern of the as-prepared sample. The wavelength is 0.5391 Å. (b) The bright-field TEM image of the as-prepared sample. There are also many chaotic stress lines that may be introduced in the sample preparation. (c) The SAED image of the region marked as A in (b). It can be well indexed as the $[111]$ zone axis pattern of the β -Ti phase. (d) The HRTEM image of the region marked as B in (b). The totally disordered feature confirms its amorphous structure. The scale bars are 0.5 μm in (b), 5 nm^{-1} in (c), and 10 nm in (d).

characteristic length scale of the composite sample. Therefore, the XRD data are statistically reliable but basically without spatial resolution. With the fast development of advanced x-ray techniques, two-dimensional mapping of the amorphous phase with spatial resolution is possible using a sub-micrometer x-ray beam and very thin samples. In this work, to reveal the details of the composite structures at the microscopic level, TEM experiments were performed instead. Figure 1(b) is the bright-field TEM image of the specimen. It is apparent that there are two typical regions with distinct contrast, including a white region marked as B and the other gray regions marked as A. Figure 1(c) is the SAED image of the region marked as A in Fig. 1(b), which can be indexed to the $[111]$

zone axis pattern of the β -Ti phase. Figure 1(d) is an HRTEM image of the region marked as B in Fig. 1(b). The completely disordered atomic arrangement indicates an amorphous structure. Therefore, according to the synchrotron XRD and TEM results, we confirm the co-existence of an amorphous phase and a β -Ti phase reproduced in the as-prepared $\text{Ti}_{59.1}\text{Zr}_{37}\text{Cu}_{2.3}\text{Fe}_{1.6}$ alloy.

Figure 2(a) shows the XRD patterns of the $\text{Ti}_{59.1}\text{Zr}_{37}\text{Cu}_{2.3}\text{Fe}_{1.6}$ alloy in a DAC as a function of pressure up to ~ 39.6 GPa during compression and decompression. All the peaks from the β -Ti phase

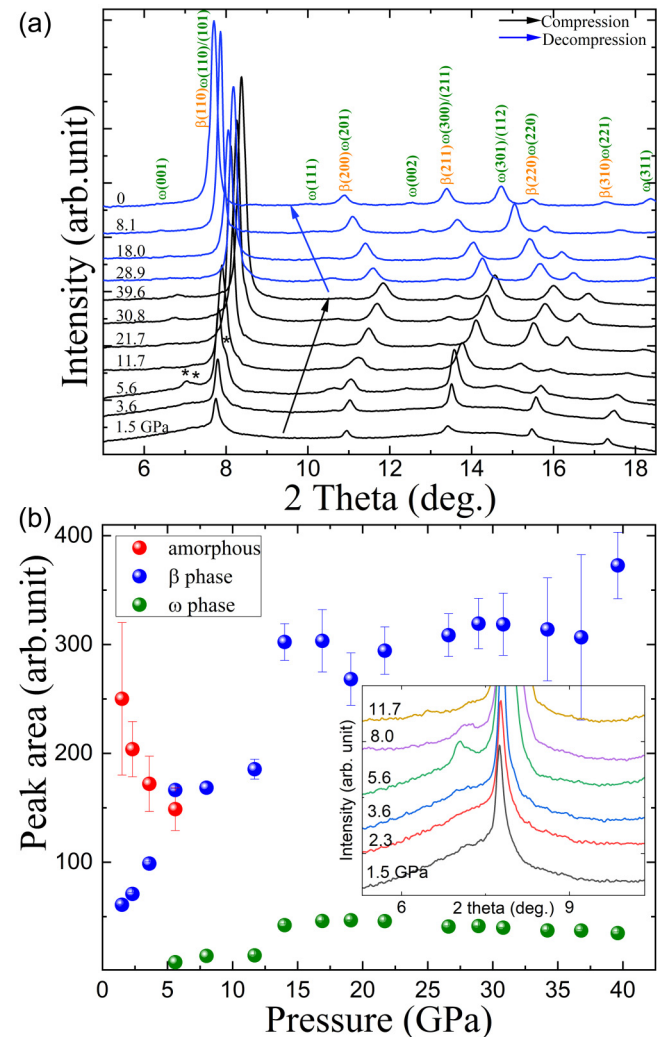


FIG. 2. *In situ* high-pressure XRD measurements of the $\text{Ti}_{59.1}\text{Zr}_{37}\text{Cu}_{2.3}\text{Fe}_{1.6}$ alloy. (a) *In situ* high-pressure XRD patterns at different pressures up to ~ 39.6 GPa during compression and decompression at room temperature. The asterisk symbols denote an unresolved α -like intermediate phase. The x-ray wavelength is 0.3220 Å. (b) The diffraction peak areas of the amorphous peak, all the peaks of the β -Ti phase, and the ω phase as a function of pressure. The inset is a zoomed image to highlight the relative weak signal from the amorphous phase as a function of pressure up to 11.7 GPa.

shift to higher two-theta angles during compression and return back to lower angles during decompression; meanwhile, the peak intensity of the β -Ti phase varies with pressure. Also, it is obvious that the broad amorphous peak beneath the (110) peak of the β -Ti phase dramatically weakens with increasing pressure and becomes almost invisible above ~ 8 GPa. Some new peaks emerge at ~ 5.6 GPa during compression, which indicates the occurrence of a pressure-induced phase transition. The peaks at $\sim 10.6^\circ$, $\sim 12.5^\circ$, and $\sim 14.6^\circ$ at 5.6 GPa can be well indexed into the (111) peak, (002) peak, and (301)/(112) peak of the ω phase. A phase accounting for the weak peaks located at $\sim 7^\circ$ and $\sim 8^\circ$ at 5.6 GPa [marked by asterisk symbols in Fig. 2(a)] is most likely the α phase but cannot be exclusively identified only by three weak peaks, and it quickly disappears below ~ 11.7 GPa. With increasing pressure, the intensity of the (301)/(112) peak of the ω -phase gets slightly stronger. When pressure is fully released, the ω phase persists and co-exists with the β -Ti phase.

The disappearance of the amorphous signal demonstrates that the $\text{Ti}_{59.1}\text{Zr}_{37}\text{Cu}_{2.3}\text{Fe}_{1.6}$ martensite amorphous alloy is not stable under high pressure. A pressure-induced crystallization of the amorphous alloy should take place during compression. However, since some weak new peaks also emerge at ~ 5.6 GPa and simultaneously the peak intensity of the initial β -Ti phase increases, which phase does the amorphous phase convert into is not clear. To address this question, it is necessary to carefully analyze the changes of the content of both the β -Ti phase and the amorphous phase below ~ 8 GPa and the correlation between them. By fitting the peak areas of the β -Ti phase and the amorphous phase, the phase content as a function of pressure is obtained, as shown in Fig. 2(b). The amorphous peak area decreases rapidly with pressure from the very beginning and almost disappears above ~ 8 GPa, while peak areas of the β -Ti phase increases continuously. Below ~ 5.6 GPa, no other crystalline phase forms, therefore, the opposite trends of the phase content variations of the amorphous phase, and the β -Ti phase indicates that the amorphous phase destabilizes and most likely converts into the β -Ti phase during compression.

Above ~ 5.6 GPa, the ω -Ti phase also starts to emerge. Since not much amorphous phase is left above 5.6 GPa, it is most likely that the traditional martensitic phase transition from β -Ti to ω -Ti, which is inhibited by the high local elastic strain energy at ambient conditions is activated by high pressure. However, this β -Ti to ω -Ti phase transition is quite sluggish. The β -Ti and ω -Ti phases co-exist over a wide pressure range of up to ~ 40 GPa during compression and also decompression. In contrast to the weak signal of the ω -Ti phase, the β -Ti phase shows sharp and well-defined diffraction peaks, which enables us to accurately refine the interplanar d -spacings, its unit cell parameters, and volume as a function of pressure. The unit cell volume as a function of pressure can be well fitted by the third-order Birch–Murnaghan equation of state (EOS),³¹ which yields the isothermal bulk modulus at ambient pressure $B_0 = 105(5)$ GPa and its derivative $B'_0 = 2.9(8)$. The bulk modulus obtained for this $\text{Ti}_{59.1}\text{Zr}_{37}\text{Cu}_{2.3}\text{Fe}_{1.6}$ alloy is close to the value of ~ 96 GPa of a β -Ti phase in other Ti-based alloys.²⁴

The sample recovered from the high-pressure experiment was further characterized by TEM, as shown in Fig. 3. In Fig. 3(a), the bright-field TEM image shows no area with bright contrast any more, such as that in Fig. 1(b), which confirms the disappearance

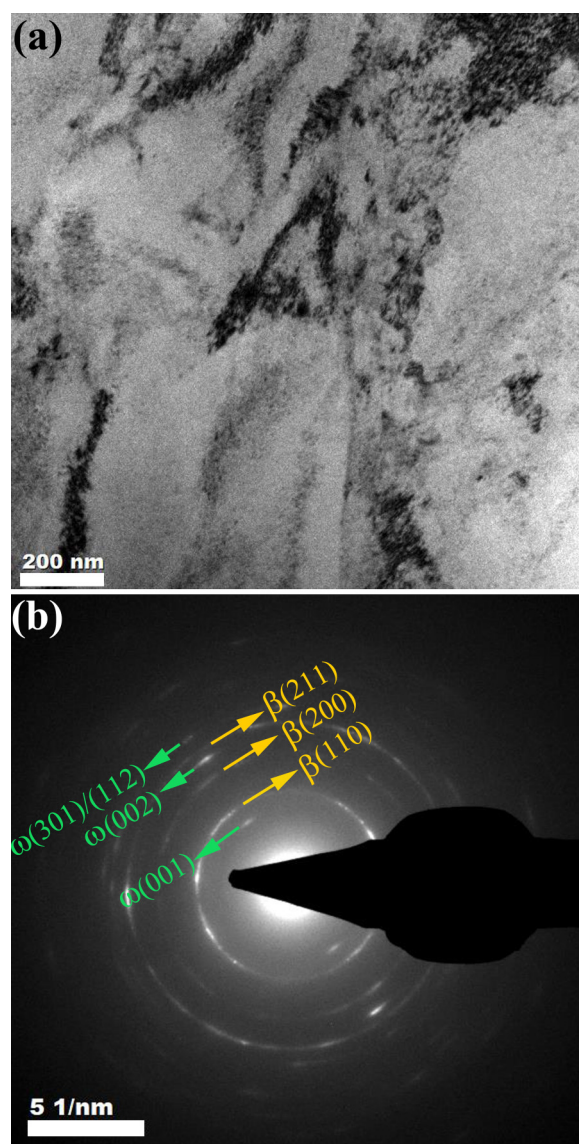


FIG. 3. TEM characterization of the recovered sample after a high-pressure experiment up to ~ 40 GPa. (a) The bright-field TEM image and (b) the SAED pattern of the entire area as shown in (a). The scale bars are 200 nm in (a) and 5 nm^{-1} in (b).

of the amorphous phase due to irreversible pressure-induced crystallization. Instead, the SAED pattern [Fig. 3(b)] of the specimen evidences the existence of the major β -Ti phase and the relative weak ω -Ti phase, as observed by *in situ* high-pressure XRD.

What destabilizes the $\text{Ti}_{59.1}\text{Zr}_{37}\text{Cu}_{2.3}\text{Fe}_{1.6}$ martensite amorphous alloy and results in devitrification? It has been suggested by Zhang *et al.*¹⁹ that the formation of the martensite amorphous alloy may be a resultant of the high local elastic strain energy. However, the local elastic strain was not quantitatively estimated.

Actually, it has been well recognized that local atomic level strain does play a dominant role in the formation of conventional amorphous alloys.^{32–34} Egami and Waseda proposed a topological instability model to account for the formation of binary metallic glasses,³² in which the atomic size difference contributes to the local atomic strain and high strain favors the formability of metallic glasses, expressed as $C_b^{min} |(r_b/r_a)^3 - 1| \approx 0.1$, where C_b^{min} is the critical minimum solute concentration and r_a and r_b are the atomic radii of the solvent and solute, respectively. Furthermore, Salisboa *et al.* extended the model to multicomponent systems and introduced a λ criterion,³⁴ expressed as $\lambda = \sum_{i=B}^Z C_i \left| \left(\frac{r_i}{r_a} \right)^3 - 1 \right|$, where C_i is the solute concentration, r_a and r_i are the atomic radii of the solvent and solute atoms, respectively, and $\lambda > 0.1$ favors the formation of an amorphous structure.

For the $\text{Ti}_{59.1}\text{Zr}_{37}\text{Cu}_{2.3}\text{Fe}_{1.6}$ alloy, Ti with highest concentration is considered as the solvent, and the others are solutes. Taking the high-pressure volume data of the four constituent elements from the literature,^{35–39} the parameter λ can be calculated to estimate the local strain of the alloy as a function of pressure (as shown in Fig. 4). It is clear that the amorphous structure gets less stable during compression since λ decreases with increasing pressure, eventually destabilized at ~ 41 GPa when λ equals 0.1. The right y-axis of Fig. 4 shows the value of $|(r_i/r_a)^3 - 1|$ and presents the relative atom volume difference between each solute atom and the solvent Ti as a function of pressure. $|(r_{\text{Fe}}/r_{\text{Ti}})^3 - 1|$ and $|(r_{\text{Cu}}/r_{\text{Ti}})^3 - 1|$ are much larger than $|(r_{\text{Zr}}/r_{\text{Ti}})^3 - 1|$; however, the former two change little with pressure, while $|(r_{\text{Zr}}/r_{\text{Ti}})^3 - 1|$ decreases sharply with pressure and dominates the change of λ due to the high concentration of the solute Zr.

In our experiments, the crystallization occurs below ~ 8 GPa, which is much lower than the predicted pressure of ~ 41 GPa

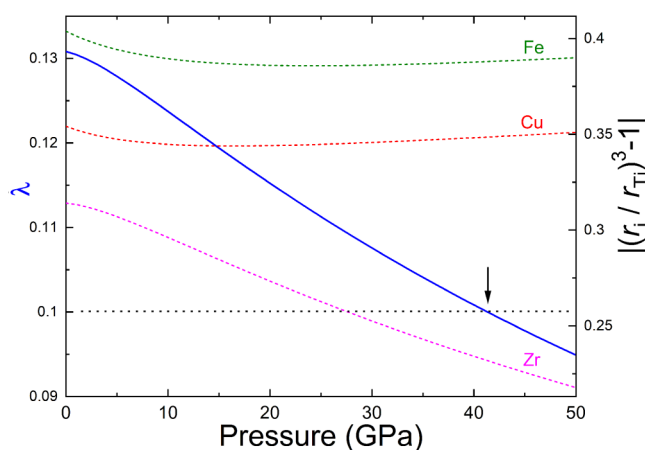


FIG. 4. Estimation of the relative volume difference between the solute and solvent atoms in the $\text{Ti}_{59.1}\text{Zr}_{37}\text{Cu}_{2.3}\text{Fe}_{1.6}$ alloy as a function of pressure. The left y-axis shows the λ parameter as a function of pressure (blue solid curve). The right y-axis presents the separate contribution from each solute atom to the λ parameter as a function of pressure (dashed lines). The dotted horizontal line marks the position where $\lambda = 0.1$.

according to the local atomic strain model. It should be noted that the atomic radii taken from high-pressure data of pure elements may be different from that of complex multi-component amorphous alloys. Moreover, the parameter λ is also semi-empirical,³² which may be responsible for the large deviation of critical pressure. The predicted destabilization trend as the increasing pressure of the $\text{Ti}_{59.1}\text{Zr}_{37}\text{Cu}_{2.3}\text{Fe}_{1.6}$ alloy is consistent with the experimental observation, providing us an atomic level insight into the mechanism of the pressure-induced crystallization of the martensite amorphous alloy.

IV. CONCLUSION

In summary, *in situ* high-pressure XRD studies on the $\text{Ti}_{59.1}\text{Zr}_{37}\text{Cu}_{2.3}\text{Fe}_{1.6}$ martensitic amorphous alloy have been performed up to ~ 39.6 GPa during compression and decompression at room temperature. Although the amorphous martensite phase is believed to be more stable than the β -Ti phase and also other typical α' , α'' , or ω martensites during cooling suggested by a heat release accompanying its formation,¹⁹ the *in situ* XRD results demonstrate that the amorphous martensite phase is not stable at all under high pressure and will quickly transform into the β -Ti phase below 8 GPa. These results reveal a pressure-induced crystallization of an amorphous phase at room temperature, which was seldom observed in amorphous alloys before. The large difference of atomic radii between the solute Zr and solvent Ti is found to dominate the stabilization of the amorphous structure. With increasing pressure, the difference in atomic radii between Zr and Ti quickly decreases, which eventually causes crystallization. These results also suggest that pressure is a powerful and clean parameter to tune the local atomic elastic strain/stress and destabilize/stabilize various martensite phases. More studies in the future employing high pressure on martensite amorphous alloys could help to tailor their structure and properties and further deepen our understanding of the mechanism of martensite amorphization, inverse melting, and crystallization.

ACKNOWLEDGMENTS

The authors thank Dr. Yanjun Li from the Shanghai Institute of Measurement and Testing Technology (SIMT) for her kind help with the TEM measurements. This work was supported by the National Natural Science Foundation of China (NNSFC; Grant Nos. 51871054 and U1930401) and the Fundamental Research Funds for the Central Universities. This research used the beamline 13-ID-D at APS. The usage of the beamline 13-ID-D (GeoSoilEnviroCARS) at APS was supported by the National Science Foundation (NSF)-Earth Sciences (No. EAR-1634415) and the Department of Energy (DOE)-GeoSciences (No. DE-FG02-94ER14466). APS was supported by the DOE, Office of Science, Office of Basic Energy Sciences, under Contract No. DE-AC02-06CH11357. Portions of this work used the beamline 15U1 at SSRE, China and the beamline 12.2.2 at ALS, USA. ALS was supported by the Director, Office of Science, DOE-BES under Contract No. DE-AC02-05CH11231.

DATA AVAILABILITY

The data that support the findings of this study are available from the corresponding author upon reasonable request.

REFERENCES

- ¹W. Klement, R. H. Willens, and P. O. L. Duwez, *Nature* **187**, 869 (1960).
- ²A. L. Greer, *Science* **267**, 1947 (1995).
- ³W. H. Wang, C. Dong, and C. H. Shek, *Mater. Sci. Eng. R Rep.* **44**, 45 (2004).
- ⁴A. L. Greer and E. Ma, *MRS Bull.* **32**, 611 (2007).
- ⁵A. Inoue and N. Nishiyama, *MRS Bull.* **32**, 651 (2007).
- ⁶J. Schroers, *Adv. Mater.* **22**, 1566 (2010).
- ⁷X. H. Lin and W. L. Johnson, *J. Appl. Phys.* **78**, 6514 (1995).
- ⁸A. Inoue, *Acta Mater.* **48**, 279 (2000).
- ⁹J. H. Na, M. D. Demetriou, M. Floyd, A. Hoff, G. R. Garrett, and W. L. Johnson, *Proc. Natl. Acad. Sci. U.S.A.* **111**, 9031 (2014).
- ¹⁰X. L. Yeh, K. Samwer, and W. L. Johnson, *Appl. Phys. Lett.* **42**, 242 (1983).
- ¹¹R. B. Schwarz and W. L. Johnson, *Phys. Rev. Lett.* **51**, 415 (1983).
- ¹²C. C. Koch, O. B. Cavin, C. G. McKamey, and J. O. Scarbrough, *Appl. Phys. Lett.* **43**, 1017 (1983).
- ¹³L. E. Rehn, P. R. Okamoto, J. Pearson, R. Bhadra, and M. Grimsditch, *Phys. Rev. Lett.* **59**, 2987 (1987).
- ¹⁴W. Johnson, *Prog. Mater. Sci.* **30**, 81 (1986).
- ¹⁵I. Apachitei, L. M. Craus, and G. Calugaru, *J. Alloys Compd.* **260**, 135 (1997).
- ¹⁶M. Dilixiati, K. Kanda, K. Ishikawa, and K. Aoki, *J. Alloys Compd.* **337**, 128 (2002).
- ¹⁷J. Y. Huang, Y. T. Zhu, X. Z. Liao, and R. Z. Valiev, *Philos. Mag. Lett.* **84**, 183 (2004).
- ¹⁸Y. Zhu, G. Liao, T. Shi, Z. Tang, and M. Li, *Acta Mater.* **125**, 69 (2017).
- ¹⁹L. Zhang, H. Zhang, X. Ren, J. Eckert, Y. Wang, Z. Zhu, T. Gemming, and S. Pauly, *Nat. Commun.* **9**, 506 (2018).
- ²⁰A. Dewaele, V. Stutzmann, J. Bouchet, F. Bottin, F. Occelli, and M. Mezouar, *Phys. Rev. B* **91**, 134108 (2015).
- ²¹W. Sha and S. Malinov, *Titanium Alloys: Modelling of Microstructure, Properties and Applications* (Elsevier Science, 2009).
- ²²Y. K. Vohra, S. K. Sikka, S. N. Vaidya, and R. Chidambaram, *J. Phys. Chem. Solids* **38**, 1293 (1977).
- ²³Y. B. Wang, Y. H. Zhao, Q. Lian, X. Z. Liao, R. Z. Valiev, S. P. Ringer, Y. T. Zhu, and E. J. Lavernia, *Scr. Mater.* **63**, 613 (2010).
- ²⁴D. Smith, O. P. J. Joris, A. Sankaran, H. E. Weekes, D. J. Bull, T. J. Prior, D. Dye, D. Errandonea, and J. E. Proctor, *J. Phys. Condens. Matter* **29**, 155401 (2017).
- ²⁵Q. Zeng, W. L. Mao, H. Sheng, Z. Zeng, Q. Hu, Y. Meng, H. Lou, F. Peng, W. Yang, S. V. Sinogeikin, and J.-Z. Jiang, *Appl. Phys. Lett.* **102**, 171905 (2013).
- ²⁶Q. Zeng, H. Sheng, Y. Ding, L. Wang, W. Yang, J.-Z. Jiang, W. L. Mao, and H.-K. Mao, *Science* **332**, 1404 (2011).
- ²⁷B. Chen, J.-F. Lin, J. Chen, H. Zhang, and Q. Zeng, *MRS Bull.* **41**, 473 (2016).
- ²⁸H.-K. Mao, B. Chen, J. Chen, K. Li, J.-F. Lin, W. Yang, and H. Zheng, *Matter Radiat. Extremes* **1**, 59 (2016).
- ²⁹Y. Fei, A. Ricolleau, M. Frank, K. Mibe, G. Shen, and V. Prakapenka, *Proc. Natl. Acad. Sci. U.S.A.* **104**, 9182 (2007).
- ³⁰S. Klotz, J.-C. Chervin, P. Munsch, and G. Le Marchand, *J. Phys. D Appl. Phys.* **42**, 075413 (2009).
- ³¹F. Birch, *J. Geophys. Res.* **57**, 227, <https://doi.org/10.1029/JZ057i002p00227> (1952).
- ³²T. Egami and Y. Waseda, *J. Non-Cryst. Solids* **64**, 113 (1984).
- ³³M. Li and W. L. Johnson, *Phys. Rev. Lett.* **70**, 1120 (1993).
- ³⁴R. D. Sa Lisboa, C. Bolfarini, W. J. Botta F, and C. S. Kiminami, *Appl. Phys. Lett.* **86**, 211904 (2005).
- ³⁵A. Dewaele, P. Loubeyre, and M. Mezouar, *Phys. Rev. B* **70**, 094112 (2004).
- ³⁶A. Dewaele, P. Loubeyre, F. Occelli, M. Mezouar, P. I. Dorogokupets, and M. Torrent, *Phys. Rev. Lett.* **97**, 215504 (2006).
- ³⁷D. Errandonea, Y. Meng, M. Somayazulu, and D. Häusermann, *Physica B* **355**, 116 (2005).
- ³⁸D. A. Young, H. Cynn, P. Söderlind, and A. Landa, *J. Phys. Chem. Ref. Data* **45**, 043101 (2016).
- ³⁹Y. Zhao, J. Zhang, C. Pantea, J. Qian, L. L. Daemen, P. A. Rigg, R. S. Hixson, G. T. Gray, Y. Yang, L. Wang, Y. Wang, and T. Uchida, *Phys. Rev. B* **71**, 184119 (2005).